HHS Public Access

Author manuscript

Magn Reson Med. Author manuscript; available in PMC 2020 May 01.

Published in final edited form as:

Magn Reson Med. 2019 May ; 81(5): 2915–2923. doi:10.1002/mrm.27663.

Improved CEST Imaging with Real-Time Frequency Drift Correction

Ruibin Liu[1,*], **Hongxi Zhang**[2,*], **Weiming Niu**[2], **Can Lai**[2], **Qiuping Ding**[1], **Weibo Chen**[3], **Sayuan Liang**[4], **Jinyuan Zhou**[5], **Dan Wu**[1,5], and **Yi Zhang**[1,5]

[1]Key Laboratory for Biomedical Engineering of Ministry of Education, Department of Biomedical Engineering, College of Biomedical Engineering & Instrument Science, Zhejiang University, Hangzhou, Zhejiang, China

[2]Department of Radiology, Children's Hospital, Zhejiang University School of Medicine, Hangzhou, Zhejiang, China

[3]Philips Healthcare, Shanghai, China

[4]Clinical Research Board, Philips Research China, Shanghai, China

[5]Department of Radiology, Johns Hopkins University, Baltimore, Maryland, USA

Abstract

Purpose: To investigate the effects of frequency drift on chemical exchange saturation transfer (CEST) imaging at 3T, and to propose a new sequence for correcting artifacts due to B_0 drift in real time.

Theory and Methods: A frequency-stabilized CEST (FS-CEST) imaging sequence was proposed by adding a frequency stabilization module to the conventional non-frequency-stabilized CEST (NFS-CEST) sequence, which consisted of a small tip angle radiofrequency excitation pulse and readout of three non-phase-encoded *k* space lines. Experiments were performed on an egg white phantom and 26 human subjects on a heavy-duty clinical scanner, in order to compare the difference of FS-CEST and NFS-CEST sequences for generating the z-spectrum, magnetization transfer ratio asymmetry (MTR_{asym}) spectrum and amide proton transfer weighted (APTw) image.

Results: The B_0 drift in CEST imaging, if not corrected, would cause APTw images and MTR_{asym} spectra from both the phantom and volunteers to be either significantly higher or lower than the true values, depending on the status of the scanner. The FS-CEST sequence generated substantially more stable MTR_{asym} spectra and APTw images than the conventional NFS-CEST sequence. Quantitatively, the compartmental-average APTw signals (mean ± standard deviation) from frontal white matter regions of all 26 human subjects were −0.32% ± 2.32% for the NFS-CEST sequence, and −0.14% ± 0.37% for the FS-CEST sequence.

Conclusions: The proposed FS-CEST sequence provides an effective approach for B_0 drift correction without additional scan time, and should be adopted on heavy-duty MRI scanners.

Address for correspondence: Yi Zhang, PhD, Room 322, Zhou Yiqing Building, Yuquan Campus, Zhejiang University, 38 Zheda Road, Hangzhou 310027, China, yizhangzju@zju.edu.cn.

*Ruibin Liu and Hongxi Zhang contributed equally to this work.

Keywords

chemical exchange saturation transfer (CEST); frequency drift; frequency stabilized CEST (FS-CEST); amide proton transfer (APT)

INTRODUCTION

Chemical Exchange Saturation Transfer (CEST) imaging is an emerging molecular imaging technique (1–3). The CEST contrast is generated by saturating the exchangeable solute protons, which saturated magnetization of the solute protons will be transferred to the water protons by the chemical exchange process, leading to a reduction in the magnetization of bulk water protons. With the CEST technique, endogenous low-concentration biomolecules possessing water-exchangeable protons can be detected with a significantly enhanced sensitivity (4–6). For example, amide proton transfer (APT) imaging, a subtype of CEST imaging techniques, can detect endogenous cytosolic proteins and peptides by saturation of the amide protons in the peptide bounds (7–12). However, APT or CEST imaging is highly susceptible to the main field (B_0) inhomogeneity for magnetization transfer ratio asymmetry (MTR_{asym}) analysis(7,13,14), due to the fact that the CEST z-spectrum is acquired with a series of frequency-selective radiofrequency (RF) pulses (1,15).

Although subject motion, respiration and cardiac activity can cause small B_0 drift, the B_0 field is generally stable. However, heating of shim elements induced by eddy currents and mechanical vibrations (16,17) can lead to severe B_0 drift, which is typically encountered in the echo planar imaging (EPI) sequences that require rapid gradient switching such as those used for diffusion imaging. Furthermore, B_0 drift will not only occur during the EPI acquisition, but also continue for a considerable amount of time after the EPI acquisition until the shim elements completely cool down (17). B_0 drift can cause image shift in the phase-encoding direction of EPI readout (16–19) and compromise the efficacy of lipid suppression (20), leading to potentially significant lipid artifacts. As a consequence, if one performs a CEST imaging scan not long after an EPI acquisition, the performance of CEST imaging can be greatly influenced. Although the image shift can be corrected by post-processing in *k* space (16,17,21–24) or image space (19,25,26), ineffectiveness of lipid suppression remains a challenging problem, especially for CEST imaging (27), which cannot be solved only by post-processing. In addition, B_0 drift will cause conventional B_0 correction methods, e.g. WASSR (28), to fail for CEST imaging since it only corrects spatial B_0 inhomogeneity.

Several prior studies have attempted to correct B_0 drift in real time or post-processing. For example, Thomas et al. (20) adjusted the center frequencies of all RF pulses executed in real time via two measured non-phase-encoded *k* space lines during EPI acquisition for diffusion imaging at 1.5T. Windschuh et al. (29) introduced a post-processing correction method of B_0 drift for 3D CEST acquisition utilizing a gradient echo (GRE) readout at 7T. To the best of our knowledge, there is no real-time B_0 drift correction method introduced or implemented for CEST imaging so far. In this study, we proposed a real-time frequency-stabilized CEST (FS-CEST) sequence by inserting a frequency stabilization module into the conventional

non-frequency-stabilized CEST (NFS-CEST) imaging sequence in order to correct B_0 drift. Compared with the conventional NFS-CEST sequence, the novel FS-CEST sequence shows substantial advantages in correcting artifacts caused by B_0 drift, especially on heavy-duty scanners.

THEORY

Frequency Stabilization Module

The FS-CEST sequence consists of four modules including frequency stabilization, CEST saturation, fat suppression (e.g. spectral pre-saturation with inversion recovery, SPIR), and readout (e.g. turbo spin echo, TSE), as shown for one repetition time (TR) cycle in Fig. 1. The FS-CEST sequence commences with an additional frequency stabilization module, in contrast with the NFS-CEST sequence. Specifically, the frequency stabilization module starts with a small-tip-angle (flip angle = α) slice-selective excitation RF pulse, and then proceeds with readout of three non-phase-encoded *k* space lines acquired at the time t_1, t_2, and t_3, respectively. The phase difference between acquired *k* space lines is used to quantify the B_0 drift value which is then corrected by adjusting the RF frequencies in the succeeding CEST saturation, fat suppression and readout modules for every TR in real time.

In details, a phase difference value for the ith readout data point, $\Delta\varphi_i$, can be calculated by Fourier transforming two acquired *k* space lines and taking complex conjugate multiplication. Then, the phase difference estimation $\overline{\varphi}_{2-1}$ (phase difference between the second and first lines) or $\overline{\varphi}_{3-2}$ (phase difference between the third and second lines) of two non-phase-encoded *k* space lines are generated by averaging every single data point phase difference—$\Delta\varphi_i$. The phase differences of $\overline{\varphi}_{2-1}$ and $\overline{\varphi}_{3-2}$ are related to frequency offsets as shown in Eqs. [1] and [2], respectively,

$$\overline{\varphi}_{2-1} = 2\pi \cdot \Delta f \cdot \Delta TE_{2-1} \quad [1]$$

$$\overline{\varphi}_{3-2} = 2\pi \cdot \Delta f \cdot \Delta TE_{3-2} = 2\pi \cdot \Delta f \cdot (\Delta TE_{2-1} + \tau) \quad [2]$$

, where Δf denotes the frequency offset from the nominal B_0 frequency after initial shimming, $\Delta TE_{2-1} = t_2 - t_1$, and τ is the extra gap duration inserted between the second and third *k* space line readout.

Two frequency offset values can be calculated from Eqs. [1] and [2], respectively, as,

$$\Delta f_{fine} = \overline{\varphi}_{2-1}/(2\pi \cdot \Delta TE_{2-1}) \quad [3]$$

$$\Delta f_{coarse} = (\bar{\varphi}_{3-2} - \bar{\varphi}_{2-1})/(2\pi \cdot \tau) \quad [4]$$

, where Δf_{fine} and Δf_{coarse} are intended to tackle relatively minor and major frequency drift values, respectively. Since ΔTE_{2-1} has to accommodate gradient ramp times and a rewinding negative gradient period between t_1 and t_2 as shown in Fig. 1, it is typically at least a couple of milliseconds long. On the contrary, τ is a gap interval and has no physical limit, and thus can be infinitesimally small. For minor frequency drift, i.e. when 2π phase wrap does not exist for either $\bar{\varphi}_{2-1}$ or $\bar{\varphi}_{3-2}$, Δf_{fine} is chosen as the frequency drift value. This is because the precision of the phase difference measured is limited, due to the presence of noise. Given a phase measurement precision, the larger the ΔTE or τ, the smaller the measurable Δf, namely, the higher the measurement precision of the frequency drift. For major frequency drift, i.e. when 2π phase wrap happens for $\bar{\varphi}_{2-1}$, Δf_{coarse} is chosen as the frequency drift value. One can test whether phase wrap occurs based on whether the difference between Δf_{fine} and Δf_{coarse} is greater than Δf_{fine}. Here, we assume no phase wrap happens for Δf_{coarse} since τ is chosen to be a very small value.

METHODS

MRI Experiments

All experiments were performed on a 3T Philips Achieva MRI scanner (Philips Healthcare, Best, The Netherlands) with a body coil for RF transmission and an 8-channel coil for reception. In the phantom study, two test tubes, one full of fresh egg white (taken directly from raw eggs) and the other one with half fresh egg white and half water, were placed inside a flask filled with 2% agarose solution. The *in vivo* study was approved by the local Institutional Review Board. Before participation in this study, written parental consent forms were obtained from all 26 subjects, including 16 males (6.0 ± 4.3 years old) and 10 females (5.5 ± 2.9 years old). The enrolled subjects were referred for MRI scanning due to idiopathic febrile seizures, headaches or dizziness, and to best of our knowledge, with no known condition that could alter the CEST index.

Data Acquisition

The imaging parameters used in the four modules of the FS-CEST sequence were as follows. As for the frequency stabilization module, the flip angle of the RF pulse was $\alpha = 3^0$, and the three non-phase-encoded *k* space lines were acquired at times of $t_1 = 2.54$ms, $t_2 = 5.12$ms, and $t_3 = 8.33$ms, with a blank interval of $\tau = 0.64$ms. These acquisition times resulted in a maximum phase-wrap-free frequency offset of 388Hz and 1563Hz for the minor and major frequency drift estimation in Eqs. [3] and [4], respectively. The CEST saturation module included four 2μ T block saturation pulses each with a 200ms duration, and a 10ms long spoiler gradient between saturation pulses with a 10mT/m amplitude (27). The SPIR fat suppression module composed of a fat-selective 110^0 RF pulse and a crusher gradient. The TSE acquisition module started with a slice-selective 90^0 excitation pulse followed by 42 slice-selective 180^0 refocusing pulses (turbo factor = 42), with TR =

3000ms, echo time = 6.7ms, SENSE (30) factor = 2, slice thickness = 5mm, field of view = 212×186mm^2, and acquisition resolution = 2.2×2.2mm^2. The NFS-CEST sequence used identical parameters to the FS-CEST one except there is no frequency stabilization module in NFS-CEST.

For both the FS-CEST and NFS-CEST sequences, 63 frequency offsets were acquired along the z-spectrum for a single slice resulting in a total scan duration of 3.2min separately. The 63 frequency offsets included an unsaturated reference scan (S_0 image) and saturated scans at 0, ±0.25, ±0.5, ±0.75, ±1, ±1.5, ±2 (2), ±2.5 (2), ±3 (2), ±3.25 (2), ±3.5 (6), ±3.75 (2), ±4 (2), ±4.5, ±5, ±6, 10, 15.625, 20, 30, 40, 50, 60, 70, and 80ppm, where the number in the parentheses referred to the number of repetitions. Densely-sampled frequency offsets around 0 ppm were intended to obtain more accurate B_0 map fitting (31), the frequency offsets between 10 and 80ppm were designed for EMR fitting (32,33), and more frequency offsets near ±3.5ppm were used to achieve high signal-to-noise ratio APT-weighted (APTw) images (7,31,34). For both phantom and human studies, the FS-CEST and NFS-CEST sequences were run consecutively at the same slice location for every case on a heavily-used clinical scanner (8am to 10pm on weekdays and 8am to 5pm on weekends) with little idle time between scans. The CEST sequences were inserted randomly throughout the day depending on availability of scan time without consideration of what sequences were run for previous subjects. However, for the same subject, CEST sequences were run before injection of contrast agents and EPI sequences.

Data Analysis

All data processing was performed using MATLAB (The MathWorks, Natick, MA). In order to correct the spatial B_0 inhomogeneity, z-spectrum data within 6ppm and −6ppm was fitted with a 12th-order polynomial on a voxel-by-voxel basis (7). Then, the fitted z-spectrum was interpolated to a 1Hz frequency resolution, and the deviation of the position with minimum water signal intensity from the nominal 0ppm frequency was defined as B_0 offset (7,34). After correcting spatial B_0 inhomogeneity effects, the APTw signal, z-spectrum and MTR_{asym} spectrum for each voxel was obtained. The APTw images of phantoms and volunteers scanned with FS-CEST and NFS-CEST sequences were compared qualitatively. For quantitative comparison, regions of interest (ROI) were chosen in egg white and agar locations for phantoms and in frontal white matter areas for humans. The mean APTw intensity, mean z-spectrum and mean MTR_{asym} spectrum from each ROI was compared between FS-CEST and NFS-CEST sequences. The paired t-test was used for statistical comparison with p-value<0.05 considered significant.

RESULTS

Figure 2 shows the APTw images, z-spectra, and MTR_{asym} spectra acquired from the same phantom in three representative runs using the FS-CEST and NFS-CEST sequences. The APTw images from the FS-CEST sequence (Figs. 2d-2f) stayed relatively stable in three repeat runs. On the contrary, the APTw images from the NFS-CEST sequence could be mostly equal to (Figs. 2a vs. 2d), higher than (Figs. 2b vs. 2e), or lower than (Figs. 2c vs. 2f) those obtained with the FS-CEST sequence. While little difference could be seen between

the z-spectra scanned with FS-CEST and those with NFS-CEST (Figs. 2g-2i), agarose MTR_{asym} spectra from the FS-CEST sequence were substantially different than those from the NFS-CEST sequence. As with the APTw images, the NFS-CEST sequence could lead to similar (Fig. 2j), elevated (Fig. 2k), or reduced (Fig. 2l) MTR_{asym} spectra compared to the FS-CEST sequence. Meanwhile, results from egg white regions (Fig. S1) were essentially consistent with those from agarose locations (Fig. 2).

Figure 3 compares the APTw images acquired from three representative subjects out of total 26 ones scanned with the FS-CEST and NFS-CEST sequences. As shown in the second row of Fig. 3, the FS-CEST sequence generated consistently stable APTw images throughout all subjects. However, the APTw signal intensity from NFS-CEST was either roughly identical to (Figs. 3a vs. 3d), greater than (Figs. 3b vs. 3e), or smaller than (Figs. 3c vs. 3f) that from FS-CEST, which coincides with the results from the phantom study as shown in Fig. 2. Notably, the NFS-CEST sequence sometimes produced abnormal APTw images falsely mimicking those from brain tumor patients (34) as in Fig. 3b. Moreover, the influence of the amplitudes of B_0 drift on the quality of APTw images is illustrated in Fig. S2.

Figure 4 displays z-spectra and MTR_{asym} spectra from frontal matter regions (delineated in Fig. 3) of the three aforementioned human subjects scanned with FS-CEST and NFS-CEST sequences. Minor difference was seen in the z-spectra between the FS-CEST and NFS-CEST sequences (Figs. 4a-4c). Again, the MTR_{asym} spectra scanned with the NFS-CEST sequence could be mostly equal to (Fig. 4d), higher than (Fig. 4e) or lower than (Fig. 4f) than those of the FS-CEST sequence, confirming the same trend seen on the APTw images in Fig. 3. In addition, the differences of APTw images, z-spectra and MTR_{asym} spectra between FS-CEST and NFS-CEST are shown in Fig. S3.

Figure 5 exhibits the means and standard deviations of APTw signals in the frontal white matter ROI from every case of the total 26 subjects using NFS-CEST (blue line) and FS-CEST (red line) sequences. Clearly, the FS-CEST sequence generated tightly bounded APTw signals in all subjects. However, the NFS-CEST sequence caused pronounced fluctuations among cases, with the maximum mean APTw intensity reaching 5% and the minimum APTw signal approaching −5%. The average and standard deviation of the mean APTw intensity from all 26 ROIs were −0.14% ± 0.37% for the FS-CEST, and −0.32% ± 2.32% for the NFS-CEST sequence. Furthermore, the FS-CEST and NFS-CEST sequences did not produce statistically significantly different mean APTw signals with a p-value of 0.71.

DISCUSSION

In this study, we proposed a novel frequency-stabilized CEST sequence by inserting a frequency stabilization module in front of the conventional non-frequency-stabilized CEST sequence in order to correct B_0 drift. The frequency stabilization module measures the B_0 frequency in every TR cycle and corrects any possible frequency offset in the succeeding CEST saturation, lipid suppression and acquisition modules in real time. As shown by the phantom (Fig. 2) and human (Figs. 3–5) results, the FS-CEST sequence demonstrated remarkably improved resilience to B_0 drift comparing with the conventional NFS-CEST

sequence. The stability of not only the APTw signals (Figs. 2, 3 and 5) but also the whole MTR_{asym} spectra (Figs. 2 and 4) was dramatically enhanced with the FS-CEST sequence. In contrast, the NFS-CEST sequence generated results that were not clinically usable in many cases (Figs. 3b and 3c). Notably, the additional time spent on the frequency stabilization module is negligible compared to the time used by the other modules in the FS-CEST sequence.

The B_0 field can have both spatial inhomogeneity and temporal instability. Here, the frequency stabilization module uses a slice-selective RF excitation pulse and non-phase-encoded readout, which means it only corrects the temporal B_0 frequency instability of the selected volume on average. On the scanner used in this study, the range of B_0 drift encountered during each 3.2min FS-CEST scan (Fig. S4) had an average value of 10.1Hz, a maximum value of 80.3Hz and a minimum value of 2.4Hz, which were well under the correction limit of 388Hz or 1536Hz provided by the frequency stabilization module. Though the frequency stabilization module cannot correct spatial B_0 inhomogeneity, the WASSR or dual-echo GRE method can be readily used to correct that. The B_0 drift is mainly due to heating of the passive shim elements, which correlates with the hardware stress of the MRI system (35). It is known that sequences such as EPI or steady-state free precession (SSFP) require rapid gradient switching and cause heating of shim elements due to eddy currents and mechanical vibrations (16,17). However, it is important to note that the induced B_0 drift can be sustained for a considerable period of time until the shim elements cool down (17). As a result, CEST sequences utilizing TSE or GRE readout will be affected if running after EPI or SSFP sequences, which will contaminate CEST metrics if not corrected for.

Numerous studies have been performed to investigate and correct the B_0 drift, especially for EPI-based sequences (16–19). But, due to the sensitivity to spatial B_0 inhomogeneity, CEST imaging has been mostly performed with TSE or GRE readout instead of EPI readout on human scanners. Recently, a retrospective correction method of the frequency drift was introduced for a 3D GRE-based gagCEST sequence, which acquired multiple M_0 phase images before, in the middle of, and after the gagCEST acquisition, and interpolated the calculated B_0 maps over time during post-processing (29). Differently, the FS-CEST sequence proposed in this study corrects the B_0 drift in real-time, and has two major advantages. First, the frequency stabilization module updates the frequency used in the succeeding lipid suppression module in real time, and thus ensures the efficacy of lipid suppression. Unlike the articular cartilage for which gagCEST has been mostly used, the human brain has a non-negligible constituent of lipid which will cause significant artifacts in CEST images if not suppressed effectively (27). The effectiveness of lipid suppression can be ensured by the prospective FS-CEST method but not the post-processing method. Second, the FS-CEST sequence uses the same scan time with the conventional NFS-CEST sequence since the frequency stabilization module takes negligible time compared to the whole TR. This means the FS-CEST sequence uses less time than the post-processing method because it does not require multiple M_0 images during the CEST acquisition. But, it is worthwhile nothing that the FS-CEST sequence can be combined with the post-processing method to achieve even better B_0 drift correction.

In this study, we have found significant artifacts using the conventional NFS-CEST sequence. However, it should be noted that our study was performed on a heavy-duty clinical scanner with essentially no gap time throughout the workday, and with frequent diffusion-weighted EPI scans. Thus, our results should not implicate any potential issue for studies done on scanners with much less work load, such as research-oriented scanners, or on scanners with infrequent EPI or SSFP acquisition. On the other hand, the CEST sequence will have to encounter harsh clinical settings if it becomes a routine clinical sequence in future. Thus, it is recommended to adopt the FS-CEST sequence in both research and clinical use. And, in any case, the FS-CEST sequence will generate equivalent results to the conventional NFS-CEST sequence when little B_0 drift exists as shown in Figs. 2a vs. 2d, and Figs. 3a vs. 3d. It is worthwhile noting that the B_0 frequency can be alternatively measured with simple free induction decay signals without readout gradients in the frequency stabilization module instead of the gradient echo signals as implemented in this work. In addition, we have mainly investigated the influence of frequency stabilization on APT imaging, and further studies on the effects of frequency stabilization should be performed for other CEST imaging methods such as GlucoCEST (36,37).

CONCLUSION

The FS-CEST sequence provides an effective method for real-time frequency stabilization and successfully corrects artifacts due to B_0 drift on APTw images and MTR_{asym} spectra in CEST imaging. The FS-CEST sequence uses the same amount of scan time with the conventional NFS-CEST sequence, and should be adopted by studies in routine clinical settings.

Supplementary Material

Refer to Web version on PubMed Central for supplementary material.

ACKNOWLEDGMENTS

NSFC grant number: 61801421. This work is also supported by “the Fundamental Research Funds for the Central Universities (Grant No. 2018QNA5016)”. NIH grant numbers: CA166171, CA228188, NS106937.

REFERENCES

1. Ward K, Aletras A, Balaban RS. A new class of contrast agents for MRI based on proton chemical exchange dependent saturation transfer (CEST). J Magn Reson 2000;143(1):79–87. [PubMed: 10698648]
2. Zhou J, van Zijl PC. Chemical exchange saturation transfer imaging and spectroscopy. Prog Nucl Magn Reson Spectrosc 2006;48(2–3):109–136.
3. Van Zijl PC, Yadav NN. Chemical exchange saturation transfer (CEST): what is in a name and what isn’t? Magn Reson Med 2011;65(4):927–948. [PubMed: 21337419]
4. Zhou J, Lal B, Wilson DA, Laterra J, Van Zijl PC. Amide proton transfer (APT) contrast for imaging of brain tumors. Magn Reson Med 2003;50(6):1120–1126. [PubMed: 14648559]
5. Jones CK, Schlosser MJ, Van Zijl PC, Pomper MG, Golay X, Zhou J. Amide proton transfer imaging of human brain tumors at 3T. Magn Reson Med 2006;56(3):585–592. [PubMed: 16892186]
6. Cai K, Haris M, Singh A, Kogan F, Greenberg JH, Hariharan H, Detre JA, Reddy R. Magnetic resonance imaging of glutamate. Nat Med 2012;18(2):302–306. [PubMed: 22270722]

7. Zhou J, Blakeley JO, Hua J, Kim M, Laterra J, Pomper MG, van Zijl PC. Practical data acquisition method for human brain tumor amide proton transfer (APT) imaging. Magn Reson Med 2008;60(4): 842–849. [PubMed: 18816868]
8. Zhang H, Kang H, Zhao X, Jiang S, Zhang Y, Zhou J, Peng Y. Amide Proton Transfer (APT) MR imaging and Magnetization Transfer (MT) MR imaging of pediatric brain development. Eur Radiol 2016;26(10):3368–3376. [PubMed: 26762941]
9. Zhang Y, Heo HY, Jiang S, Lee DH, Bottomley PA, Zhou J. Highly accelerated chemical exchange saturation transfer (CEST) measurements with linear algebraic modeling. Magn Reson Med 2016;76(1):136–144. [PubMed: 26302147]
10. Zhang Y, Heo HY, Lee DH, Zhao X, Jiang S, Zhang K, Li H, Zhou J. Selecting the reference image for registration of CEST series. J Magn Reson Imaging 2016;43(3):756–761. [PubMed: 26268435]
11. Sun PZ, Zhou J, Huang J, Van Zijl P. Simplified quantitative description of amide proton transfer (APT) imaging during acute ischemia. Magn Reson Med 2007;57(2):405–410. [PubMed: 17260362]
12. Jin T, Wang P, Zong X, Kim SG. MR imaging of the amide-proton transfer effect and the pH-insensitive nuclear Overhauser effect at 9.4 T. Magn Reson Med 2013;69(3):760–770. [PubMed: 22577042]
13. Zu Z, Janve VA, Xu J, Does MD, Gore JC, Gochberg DF. A new method for detecting exchanging amide protons using chemical exchange rotation transfer. Magn Reson Med 2013;69(3):637–647. [PubMed: 22505325]
14. Zu Z, Xu J, Li H, Chekmenev EY, Quarles CC, Does MD, Gore JC, Gochberg DF. Imaging amide proton transfer and nuclear overhauser enhancement using chemical exchange rotation transfer (CERT). Magn Reson Med 2014;72(2):471–476. [PubMed: 24302497]
15. Bryant RG. The dynamics of water-protein interactions. Annu Rev Bioph Biom 1996;25(1):29–53.
16. Thesen S, Kruger G, Muller E. Absolute correction of B0 fluctuations in echo-planar imaging. 2003 p 1025.
17. Foerster BU, Tomasi D, Caparelli EC. Magnetic field shift due to mechanical vibration in functional magnetic resonance imaging. Magn Reson Med 2005;54(5):1261–1267. [PubMed: 16215962]
18. Durand E, van de Moortele PF, Pachot-Clouard M, Le Bihan D. Artifact due to B0 fluctuations in fMRI: correction using the k-space central line. Magn Reson Med 2001;46(1):198–201. [PubMed: 11443728]
19. Kochunov PV, Liu HL, Andrews T, Gao JH, Fox PT, Lancaster JL. A B0 shift correction method based on edge RMS reduction for EPI fMRI. J Magn Reson Imaging 2000;12(6):956–959. [PubMed: 11105036]
20. Benner T, van der Kouwe AJ, Kirsch JE, Sorensen AG. Real-time RF pulse adjustment for B0 drift correction. Magn Reson Med 2006;56(1):204–209. [PubMed: 16767763]
21. Barry RL, Menon RS. Modeling and suppression of respiration-related physiological noise in echo-planar functional magnetic resonance imaging using global and one-dimensional navigator echo correction. Magn Reson Med 2005;54(2):411–418. [PubMed: 16032665]
22. Wowk B, McIntyre MC, Saunders JK. k-Space detection and correction of physiological artifacts in fMRI. Magn Reson Med 1997;38(6):1029–1034. [PubMed: 9402206]
23. Henry PG, van de Moortele PF, Giacomini E, Nauerth A, Bloch G. Field-frequency locked in vivo proton MRS on a whole-body spectrometer. Magn Reson Med 1999;42(4):636–642. [PubMed: 10502751]
24. Pfeuffer J, Van de Moortele PF, Ugurbil K, Hu X, Glover GH. Correction of physiologically induced global off-resonance effects in dynamic echo-planar and spiral functional imaging. Magn Reson Med 2002;47(2):344–353. [PubMed: 11810679]
25. Woods RP, Grafton ST, Holmes CJ, Cherry SR, Mazziotta JC. Automated image registration: I. General methods and intrasubject, intramodality validation. J Comput Assist Tomo 1998;22(1): 139–152.
26. Jenkinson M, Smith S. A global optimisation method for robust affine registration of brain images. Med Image Anal 2001;5(2):143–156. [PubMed: 11516708]

27. Zhu H, Jones CK, van Zijl PC, Barker PB, Zhou J. Fast 3D chemical exchange saturation transfer (CEST) imaging of the human brain. Magn Reson Med 2010;64(3):638–644. [PubMed: 20632402]

28. Kim M, Gillen J, Landman BA, Zhou J, van Zijl PC. Water saturation shift referencing (WASSR) for chemical exchange saturation transfer (CEST) experiments. Magn Reson Med 2009;61(6): 1441–1450. [PubMed: 19358232]

29. Windschuh J, Zaiss M, Ehses P, Lee JS, Jerschow A, Regatte RR. Assessment of frequency drift on CEST MRI and dynamic correction: application to gagCEST at 7 T. Magn Reson Med 2018;00:1–10.10.1002/mrm.27367

30. Pruessmann KP, Weiger M, Scheidegger MB, Boesiger P. SENSE: sensitivity encoding for fast MRI. Magn Reson Med 1999;42(5):952–962. [PubMed: 10542355]

31. Wen Z, Hu S, Huang F, Wang X, Guo L, Quan X, Wang S, Zhou J. MR imaging of high-grade brain tumors using endogenous protein and peptide-based contrast. Neuroimage 2010;51(2):616–622. [PubMed: 20188197]

32. Heo HY, Zhang Y, Jiang S, Lee DH, Zhou J. Quantitative assessment of amide proton transfer (APT) and nuclear overhauser enhancement (NOE) imaging with extrapolated semisolid magnetization transfer reference (EMR) signals: II. Comparison of three EMR models and application to human brain glioma at 3 Tesla. Magn Reson Med 2016;75(4):1630–1639. [PubMed: 26033553]

33. Heo HY, Zhang Y, Lee DH, Hong X, Zhou J. Quantitative assessment of amide proton transfer (APT) and nuclear Overhauser enhancement (NOE) imaging with extrapolated semi-solid magnetization transfer reference (EMR) signals: Application to a rat glioma model at 4.7 tesla. Magn Reson Med 2016;75(1):137–149. [PubMed: 25753614]

34. Zhou J, Zhu H, Lim M, Blair L, Quinones-Hinojosa A, Messina SA, Eberhart CG, Pomper MG, Laterra J, Barker PB. Three-dimensional amide proton transfer MR imaging of gliomas: initial experience and comparison with gadolinium enhancement. J Magn Reson Imaging 2013;38(5): 1119–1128. [PubMed: 23440878]

35. El-Sharkawy AM, Schär M, Bottomley PA, Atalar E. Monitoring and correcting spatio-temporal variations of the MR scanner's static magnetic field. Magnetic Resonance Materials in Physics, Biology and Medicine 2006;19(5):223–236.

36. Chan KW, McMahon MT, Kato Y, Liu G, Bulte JW, Bhujwalla ZM, Artemov D, Van Zijl PC. Natural D-glucose as a biodegradable MRI contrast agent for detecting cancer. Magn Reson Med 2012;68(6):1764–1773. [PubMed: 23074027]

37. Walker-Samuel S, Ramasawmy R, Torrealdea F, Rega M, Rajkumar V, Johnson SP, Richardson S, Gonçalves M, Parkes HG, Årstad E. In vivo imaging of glucose uptake and metabolism in tumors. Nat Med 2013;19(8):1067. [PubMed: 23832090]

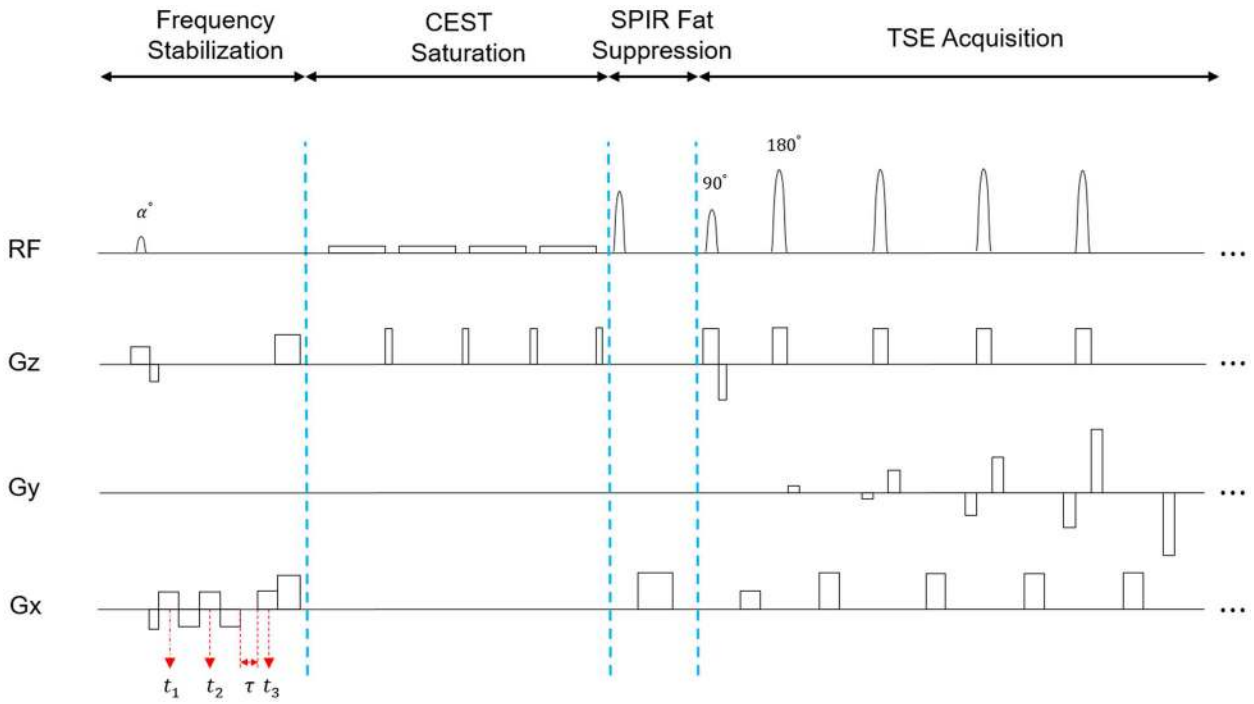

Figure 1.

Sequence diagram of FS-CEST. The sequence consists of frequency stabilization, CEST saturation, fat suppression and acquisition modules. The frequency stabilization module composes of a small-tip-angle RF excitation pulse, 3 non-phase-encoded *k* space lines acquired at t_1, t_2, t_3, and final crusher gradients.

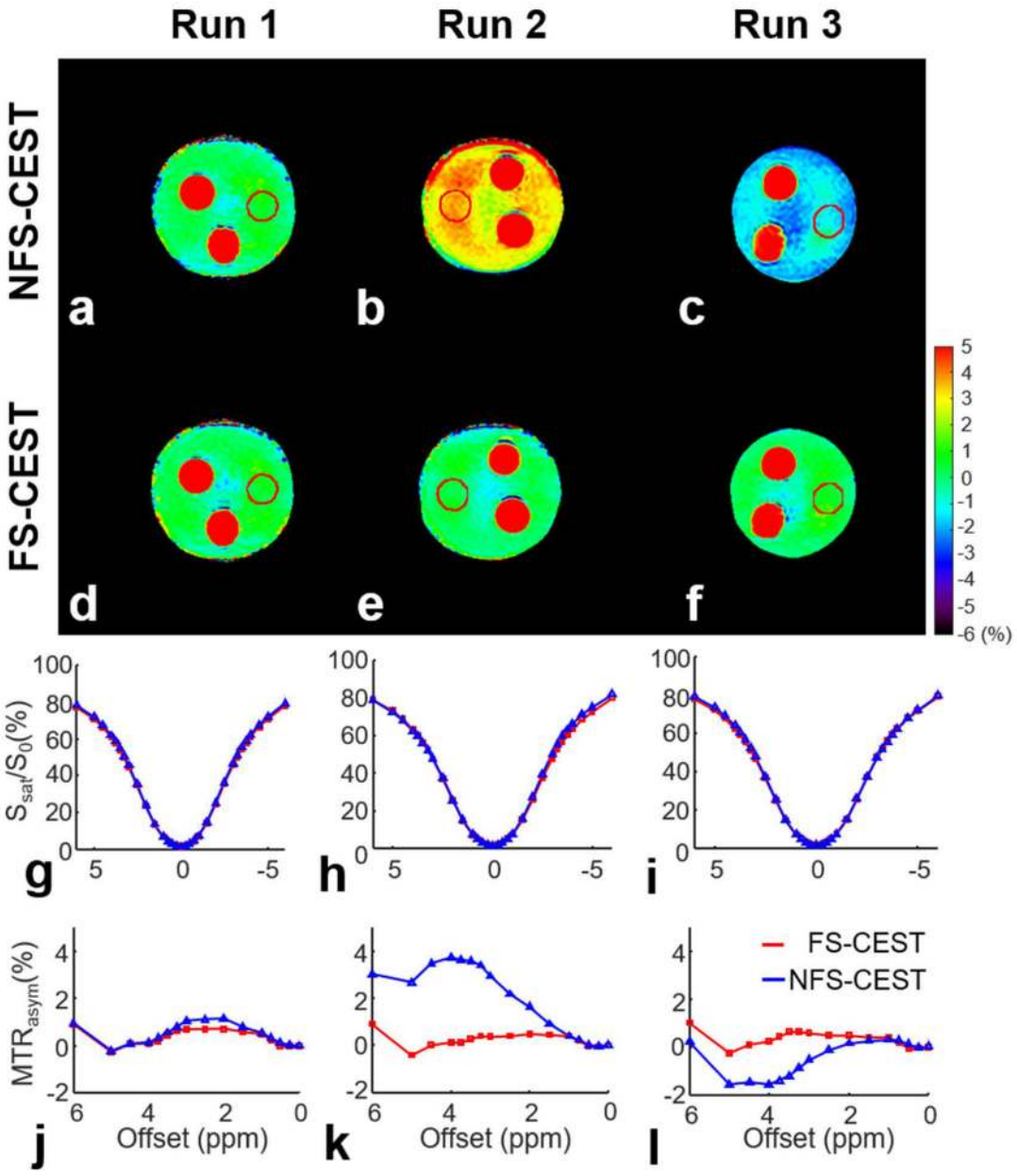

Figure 2.

Comparison of APTw images (**a**-**f**), z-spectra (**g**-**i**) and MTR_{asym} spectra (**j**-**l**) acquired from the phantom in three repeat runs using FS-CEST and NFS-CEST sequences. Each column illustrates results from one individual run of the FS-CEST and NFS-CEST sequences. The z-spectra and MTR_{asym} spectra were obtained by averaging all voxel indices from the ROI drawn in the agar region as shown in the top two rows. The red line indicates spectra from the FS-CEST sequence and the blue line denotes results from the NFS-CEST sequence.

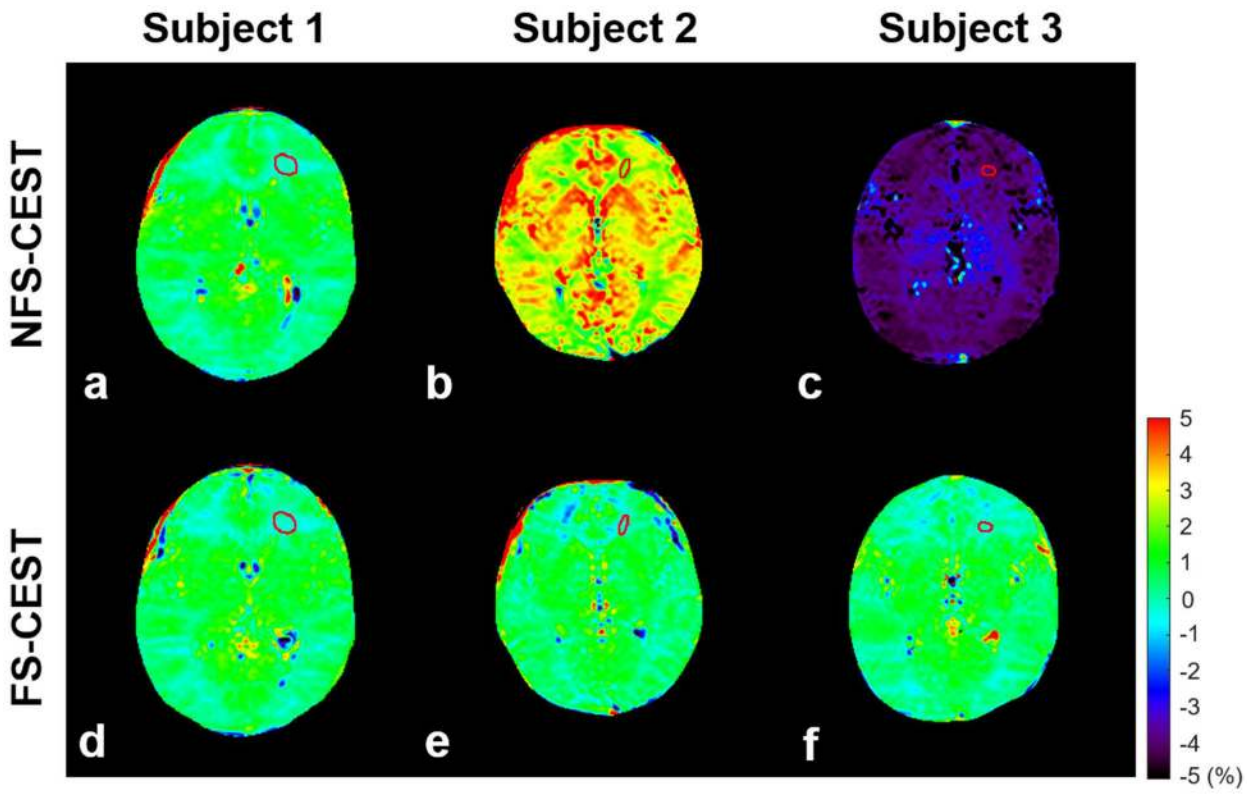

Figure 3.

Comparison of brain APTw images obtained from three representative human subjects using the NFS-CEST sequence (**a-c** in the top row) and FS-CEST sequence (**d-f** in the bottom row). Each column shows APTw images from each subject.

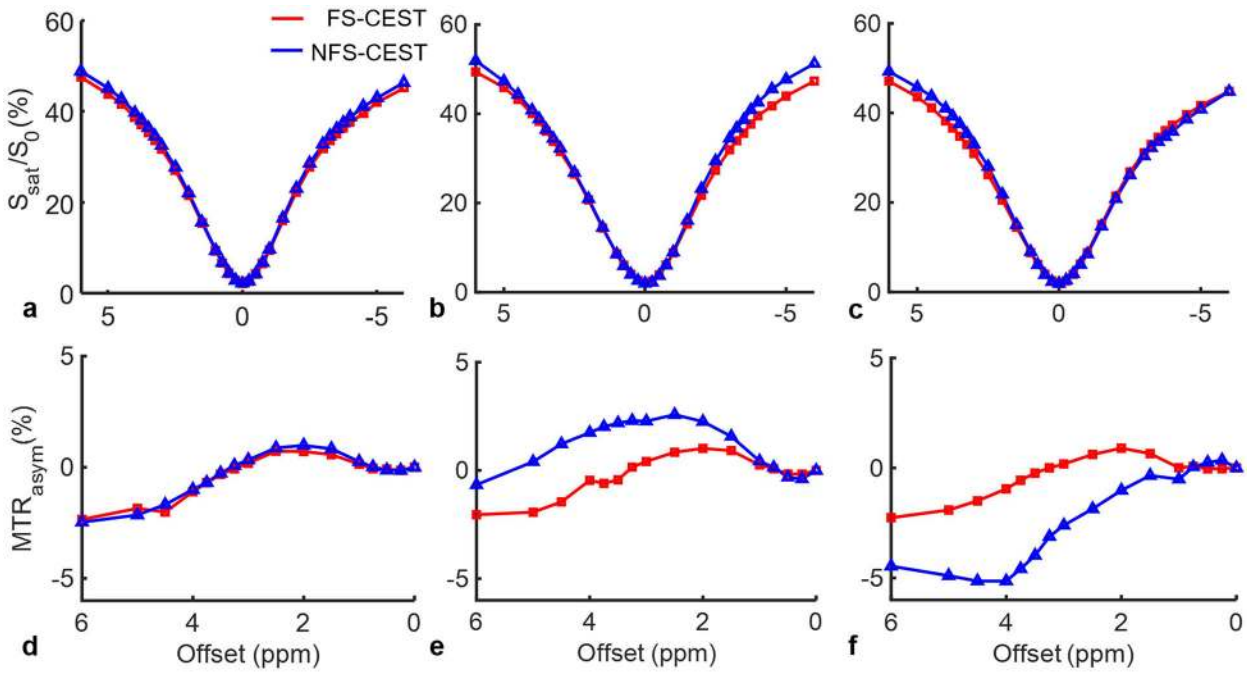

Figure 4.

Comparison of compartmental-average brain z-spectra (**a**-**c**; top row) and MTR_{asym} spectra (**d**-**f**; bottom row) acquired from the three subjects shown in Fig. 3 and from ROIs delineated by red circles in Fig. 3, using the FS-CEST sequence (red line) and NFS-CEST sequence (blue line).

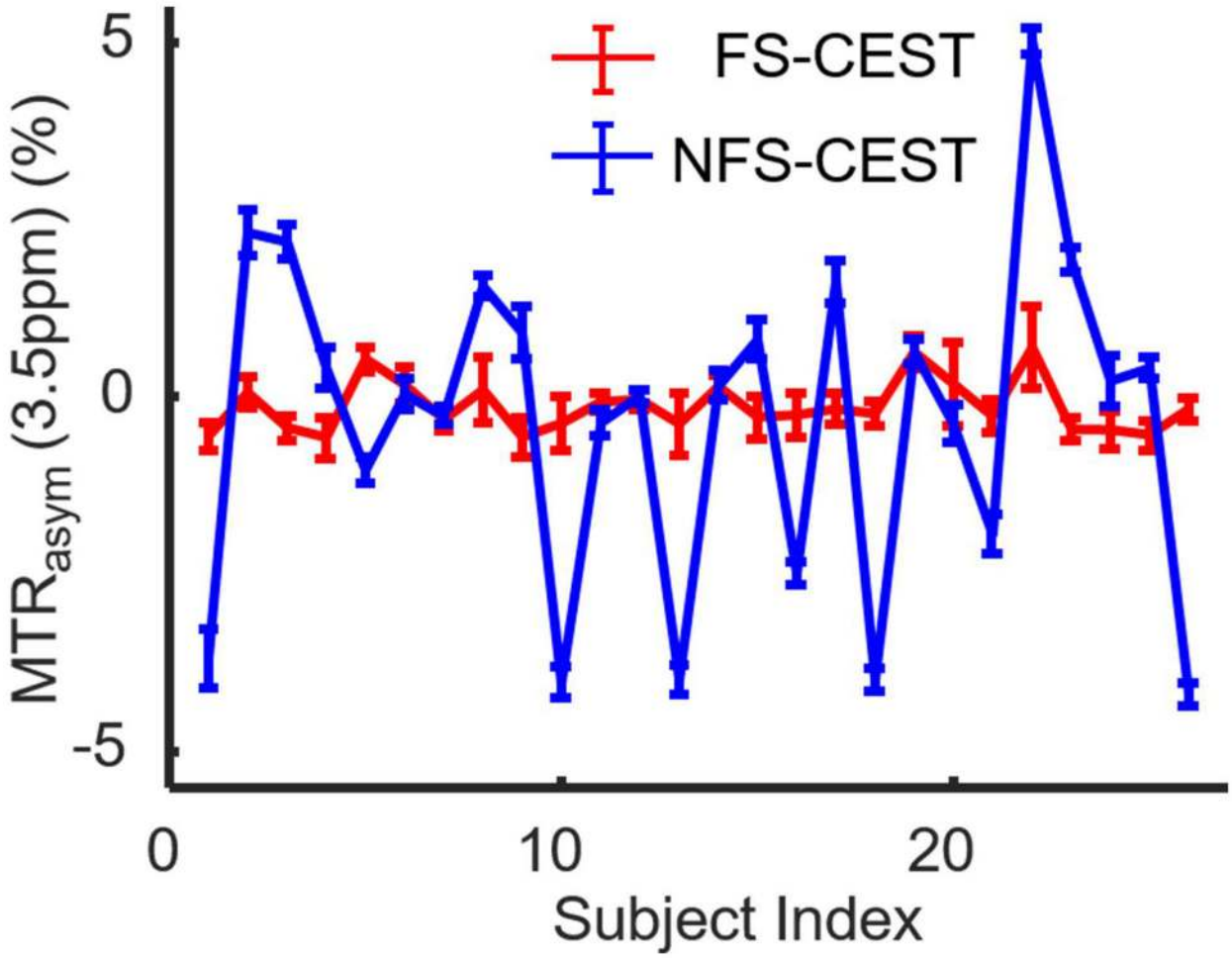

Figure 5.

APTw signals (mean ± standard deviation) from the frontal white matter ROIs of all 26 human volunteers. The horizontal axis denotes the subject index and the vertical axis denotes the APTw signal amplitude. The red line refers to results from the FS-CEST sequence, and the blue line indicates results from the NFS-CEST sequence.